



OPEN ACCESS

EDITED BY

Ángel Puga-Bernabéu,
University of Granada, Spain

REVIEWED BY

Tapan Chakraborty,
Indian Statistical Institute, India
Fei Ren,
Origin Energy, Australia

*CORRESPONDENCE

Wenhu Yu,
✉ fcywh@petrochina.com.cn
Jingwei Yu,
✉ 2016592004@cupk.edu.cn

RECEIVED 03 June 2025

REVISED 24 December 2025

ACCEPTED 30 December 2025

PUBLISHED 16 January 2026

CITATION

Yu W, Yang G, Liu J, Yeliewubai S and Yu J
(2026) Astronomical cycle identification and
high-frequency sequence stratigraphy of the
Middle Permian Lower Wuerhe Formation in
the Mahu Sag, Junggar Basin.
Front. Earth Sci. 13:1640183.
doi: 10.3389/feart.2025.1640183

COPYRIGHT

© 2026 Yu, Yang, Liu, Yeliewubai and Yu. This
is an open-access article distributed under
the terms of the [Creative Commons
Attribution License \(CC BY\)](https://creativecommons.org/licenses/by/4.0/). The use,
distribution or reproduction in other forums is
permitted, provided the original author(s) and
the copyright owner(s) are credited and that
the original publication in this journal is cited,
in accordance with accepted academic
practice. No use, distribution or reproduction
is permitted which does not comply with
these terms.

Astronomical cycle identification and high-frequency sequence stratigraphy of the Middle Permian Lower Wuerhe Formation in the Mahu Sag, Junggar Basin

Wenhu Yu^{1*}, Guo Yang¹, Jun Liu¹, Shamuhaer Yeliewubai¹ and Jingwei Yu^{2*}

¹Xinjiang Oilfield Company, Karamay, Xinjiang, China, ²Petroleum Institute, China University of Petroleum (Beijing) Karamay Campus, Karamay, Xinjiang, China

High-resolution stratigraphic analysis is essential for reconstructing sedimentary processes and constraining reservoir architecture, yet conventional methods commonly lack quantitative time control at fourth- and fifth-order (10^4 – 10^5 yr) scales. Astronomical cyclostratigraphy provides a promising approach for establishing high-resolution temporal frameworks, although orbital signals in lacustrine–deltaic systems are often obscured by tectonic and autocyclic processes. This study investigates the Middle Permian Lower Wuerhe Formation in the Mahu Sag, Junggar Basin, using high-resolution gamma-ray (GR) logs and XRF-derived Fe/Ca ratios as semi-quantitative paleoenvironmental proxies. Spectral analyses (MTM, FFT), astronomical correlation tests (COCO, eCOCO), and stratigraphic tools (INPEFA, DYNOT) were integrated to identify orbital cyclicity and construct an astrochronological framework. The analyses reveal statistically significant cyclicities consistent with Milankovitch forcing, including a dominant ~405 kyr long-eccentricity signal, subordinate ~95–125 kyr short-eccentricity components, and higher-frequency bands tentatively interpreted as obliquity (~36.0–44.3 kyr) and precession (~17.8–20.8 kyr) cycles. These cycles imply an average sedimentation rate of ~5.0–5.9 cm kyr⁻¹. Anchored by a published zircon U–Pb age of 265.4 Ma, eleven successive 405 kyr eccentricity cycles define an astronomically calibrated duration of ~4.45 Myr for the Lower Wuerhe Formation. Within this temporal framework, the formation is subdivided into three third-order transgressive–regressive (T–R) sequences (SQ1–SQ3) and further organized into eleven 405 kyr-paced high-frequency depositional cycles traceable across multiple wells. The results demonstrate that long-eccentricity forcing exerted a first-order control on high-frequency sedimentary cyclicity, providing a robust time-constrained basis for high-resolution stratigraphic correlation in lacustrine–deltaic systems.

KEYWORDS

astronomical cycle stratigraphy, astronomical timescale, high-frequency cycle, Junggar Basin, Milankovitch cycles, Permian, Wuerhe Formation

TABLE 1 Hierarchical structure of depositional cycles in the cyclostratigraphic framework and their relation to sequence stratigraphy and Milankovitch cycles [modified after (Miall and Miall, 2001)].

| Hierarchy level | Term | Duration (theoretical) | Corresponding milankovitch cycle |
|-----------------|--------------------------|------------------------|--|
| High-Order | Third-Order T-R Sequence | ~1.2–1.6 Ma | Bundles of long-eccentricity cycles ($\approx 3\text{--}4 \times 405$ ka) |
| High-Frequency | Fourth-Order cycle | ~400–405 ka | Long eccentricity cycle (~405 ka) |
| | Fifth-Order cycle | ~95–120 ka | Short eccentricity cycle (~100 ka) |
| | Sixth-Order cycle | ~30–45 ka | Obliquity cycle (~35–41 ka) |
| | Seventh-Order cycle | ~15–20 ka | Precessional cycles (~18–21 ka) |

1 Introduction

Since its introduction in the 1980s, sequence stratigraphy has provided a fundamental framework for interpreting stratigraphic continuity and discontinuity, and it is widely applied to environmental reconstruction, reservoir prediction, and basin-evolution analysis (Schlager, 2004; Miall and Miall, 2001; Catuneanu et al., 2009). By identifying regionally correlatable surfaces and organizing strata into systems tracts, sequence stratigraphy is particularly effective at first- to third-order scales ($>10^6$ yr) (Catuneanu, 2019; Catuneanu et al., 2012). As exploration increasingly demands higher-resolution correlation and predictive precision, attention has shifted to fourth- and fifth-order variability ($10^4\text{--}10^5$ yr; Table 1) (Miall and Miall, 2001). However, subdivision at these scales commonly relies on qualitative, experience-driven criteria and lacks objective, repeatable time control, limiting robust reconstruction of high-frequency stratigraphic architecture.

Cyclostratigraphy and astrochronology address this limitation by extracting orbitally paced sedimentary signals and providing quantitative time control for high-resolution analysis (Ruhl et al., 2016; Ma and Li, 2020; Zhao K. et al., 2019; Li et al., 2016; Wu et al., 2013; Boulila et al., 2014; Cao et al., 2022). Here we integrate these approaches: cyclostratigraphy supplies the primary time-based (isochronous) framework by identifying orbitally paced depositional cycles to construct an astronomical timescale, and sequence stratigraphy is then used to interpret longer-term stacking patterns and depositional trends within that temporal framework. To avoid terminological ambiguity, we explicitly adopt the Transgressive–Regressive (T-R) sequence model sensu Embry (Embry, 1993; Embry, 2002), in which sequences are bounded by maximum regressive surfaces (MRS) and comprise a transgressive systems tract (TST) and a regressive systems tract (RST) separated by a maximum flooding surface (MFS). We favor the T-R model because its surface-based definition (MRS-bounded) is compatible with identification of regionally traceable surfaces and facilitates integration with the orbitally derived framework. Consequently, high-frequency (fourth- to seventh-order) units are treated as complete depositional cycles (or cycle sets) rather than independent sequences, and high-frequency transgressive or regressive segments are described as systems-tract components (TST/RST) rather than separate “sequences.”

Milankovitch theory attributes rhythmic climate variations to periodic changes in Earth’s orbital parameters, including long eccentricity (~405 ka), short eccentricity (~100 ka),

obliquity (~41 ka), and precession (~21 ka), which can modulate sediment supply, accommodation, and preservation (Wong, 2021; Cheng et al., 2022; Lachniet et al., 2017; Slatt and Rodriguez, 2012; Xu J. et al., 2015). When preserved in sedimentary successions, such astronomically paced signals provide a quantitative basis for diagnosing high-frequency depositional rhythms and for constructing time-calibrated stratigraphic frameworks. Advances in signal-processing, including power spectral analysis and wavelet-based methods, have further strengthened the empirical rigor of cyclostratigraphic studies (Tian et al., 2022; Baddouh et al., 2016; Crampt et al., 2018; Liu et al., 2024). At the same time, variable sedimentation rates, bioturbation, compaction, and autogenic depositional processes can distort or obscure orbital signals, particularly in lacustrine–deltaic systems (Kemp and Van Manen, 2019; Laskar et al., 2004; Laskar et al., 2011). To improve detection and assess statistical significance, we employ spectral techniques such as the multitaper method (MTM) and fast Fourier transform (FFT) (Gong, 2021; Kodama and Hinnov, 2014; VanderPlas, 2018), correlation tests (COCO, eCOCO), and log-trend tools including Integrated Prediction Error Filter Analysis (INPEFA) and DYNOT, which highlight turning points and cyclic organization in well-log records (Li W. et al., 2023; Hou et al., 2021; Dang et al., 2023).

The Junggar Basin (northwest China) is a classic superimposed hydrocarbon-bearing basin with extensive lacustrine and deltaic systems. Within this basin, the Permian Wuerhe Formation is a key stratigraphic interval with favorable source–reservoir assemblages and significant exploration potential (Dang et al., 2023). Along the southern margin, third- to fourth-order stratigraphic organization in Sakmarian–Artinskian strata has been documented using seismic, wavelet analysis, and INPEFA (Li X. et al., 2023; Wang et al., 2022). In contrast, the high-frequency cyclicity and potential astronomical forcing within the Wuerhe Formation of the northern Mahu Sag remain poorly constrained; only preliminary evidence for Milankovitch pacing has been reported from the underlying Fengcheng Formation (Wang et al., 2024).

This study targets the Lower Wuerhe Formation in the Mahu Sag to (1) quantitatively identify Milankovitch-scale cyclicity in sedimentary logs, (2) construct a high-precision astronomical timescale, and (3) establish an astronomically calibrated, time-constrained stratigraphic framework for correlation. The cycle hierarchy (Table 1) follows fourth- to seventh-order organization corresponding to nominal long eccentricity (~405 ka), short eccentricity (~95–120 ka), obliquity

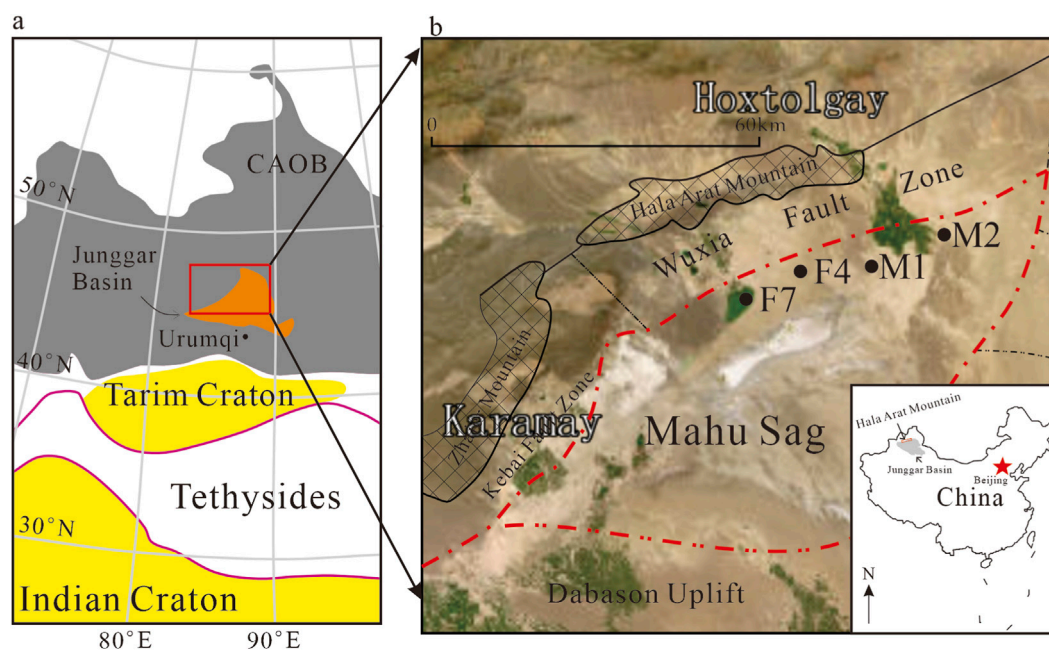


FIGURE 1
Location map of the Mahu Sag, Junggar Basin. **(a)** Regional tectonic map showing the Junggar Basin and the position of the Mahu Sag [modified after Xu XW. et al. (2015)]. **(b)** Structural boundaries of the Mahu Sag and well locations, draped on a daytime satellite image (base image: Earth Astronaut Photography Portal, public domain, <https://eol.jsc.nasa.gov/ExplorePhotos/?illum=day>).

(~30–45 ka), and precession (~15–20 ka) bands. By integrating INPEFA with multi-method spectral analyses (MTM, FFT) and correlation tests (COCO/eCOCO), we propose a reproducible workflow for recognizing high-frequency depositional rhythms in lacustrine basins, improving stratigraphic correlation, paleoclimate interpretation, and hydrocarbon-target prediction.

2 Geological background

The study area is located on the northwestern margin of the Junggar Basin in northwestern China, between the Central Asian Orogenic Belt (CAOB) and the Tarim Craton, close to the city of Karamay (Figure 1a). The Junggar Basin is a major superimposed hydrocarbon-bearing basin that preserves a thick and relatively complete sedimentary succession (Xu XW. et al., 2015; Lei et al., 2014). The Mahu Sag, developed on a pre-Carboniferous basement, is situated along the northwestern margin of the basin and was strongly modified by early Hercynian compressional and thrust tectonics (Zhao J. et al., 2019). Structurally, the sag is bounded by the Wuxia and Ke-Bai fault zones to the northwest, the Dabason Uplift to the south, and the Xiayan Uplift to the east (Figure 1b) (Tang Y. et al., 2021). On the basis of a regional unconformity between the Fengcheng and Xiazijie formations, previous studies have organized the Permian succession along the northwestern margin into two second-order sequence-stratigraphic packages (Wang et al., 2022), providing a regional framework for correlation.

This study focuses on the Lower Wuerhe Formation (P_{2w}), which is sandwiched between the Xiazijie Formation (P_{2x}) and the

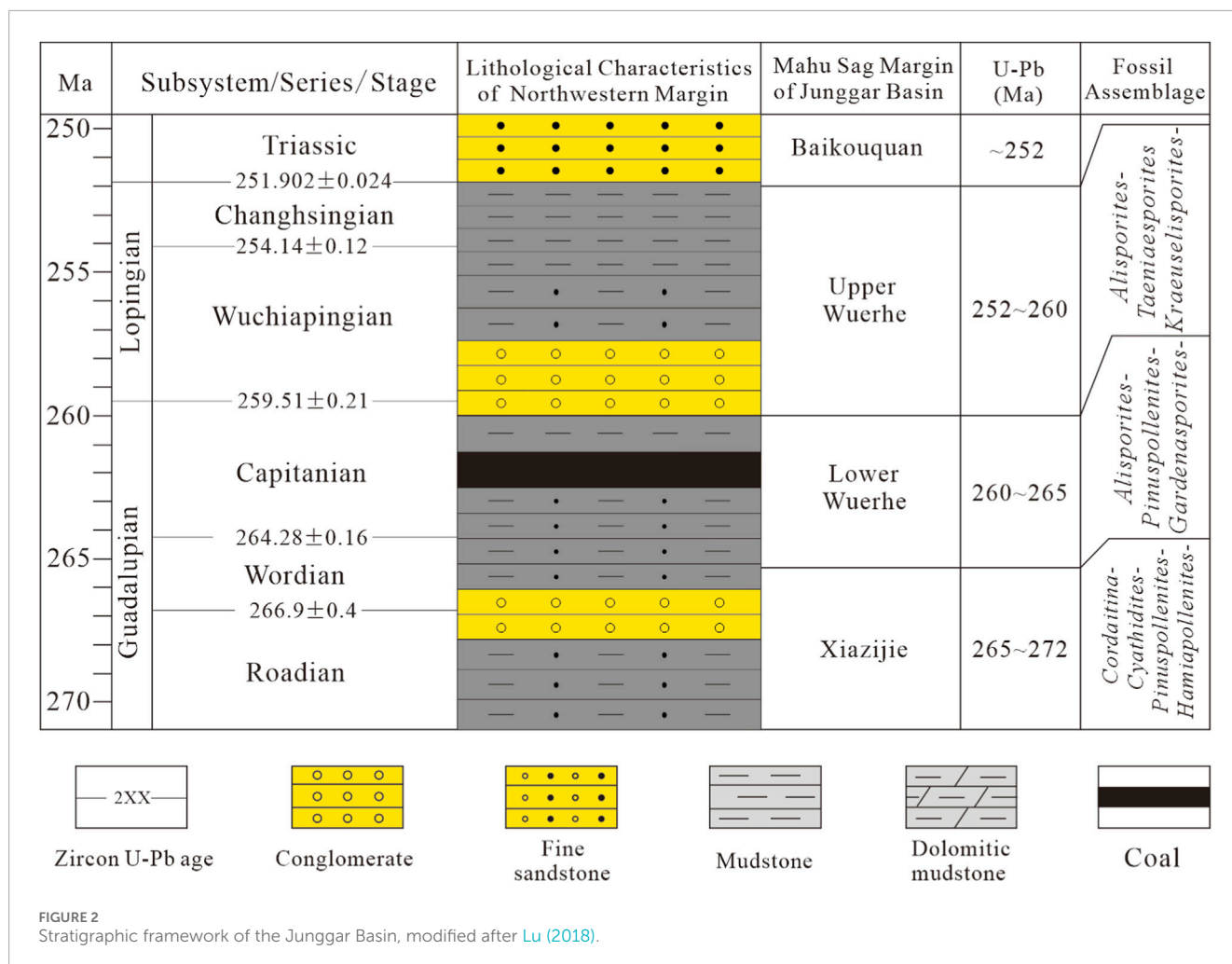
Upper Wuerhe Formation (P_{3w}) (Figure 2). Along the northwestern margin of the Junggar Basin, the Lower Wuerhe Formation is 300–700 m thick and records a transition from delta-front to shallow lacustrine environments. It shows marked lithological variability: the lower part consists mainly of mudstone and siltstone deposited in deep to semi-deep lacustrine settings; the middle part is dominated by deltaic conglomerate, sandstone, and interbedded mudstone; and the upper part again changes to mudstone- and siltstone-dominated shallow-lacustrine deposits (Tang W. et al., 2021; Yang et al., 2010).

Regional stratigraphic compilations integrating zircon U–Pb ages and fossil assemblages (Figure 2) indicate that the Xiazijie Formation spans ca. 272–265 Ma, whereas the overlying Lower Wuerhe Formation corresponds to ca. 265–260 Ma within the Capitanian Stage of the Guadalupian Series. In particular, Lu reported a youngest concordant zircon U–Pb age of 265.4 ± 3.5 Ma from tuffaceous horizons within the Lower Wuerhe succession on the northwestern margin of the Junggar Basin, supporting assignment of a late Middle Permian (Capitanian) age to the studied interval (Lu, 2018). In this study, the 265.4 ± 3.5 Ma zircon U–Pb age from the Lower Wuerhe Formation is used as the principal tie point for anchoring the floating astronomical timescale.

3 Materials and methods

3.1 Data sources and proxy selection

This study uses high-resolution gamma-ray (GR) logs (0.125 m sampling interval) from wells F7, F4, M1, and M2, together with 298 paired Fe and Ca geochemical measurements from well F7



(original 2 m spacing, resampled to 0.125 m by linear interpolation to match the log resolution), covering the Permian Lower Wuerhe Formation in the Mahu Sag, northwestern Junggar Basin. The resampling is applied only to enable point-by-point comparison and subsequent time-series analyses requiring evenly spaced data; it does not introduce additional information and may smooth the shortest-wavelength variability. All datasets were provided by Xinjiang Oilfield Company, China National Petroleum Corporation.

GR logs record the abundance of radioactive elements (U, Th, K) and are widely used to track lithological variations and infer changes in depositional environment and relative lake-level trends (Strasser et al., 2006). Clay-rich intervals typically show higher GR values due to adsorption of radioactive elements, whereas cleaner sand-rich and/or carbonate-rich intervals generally yield lower GR responses (Schnyder et al., 2006). Calcium (Ca) is commonly associated with carbonate minerals in marine or lacustrine settings and is often used as a proxy for carbonate accumulation and productivity-related dilution (Ma et al., 2020). Iron (Fe) is frequently linked to siliciclastic input and catchment weathering/erosion, and thus can reflect changes in clastic supply (Peterson et al., 2000; Govin et al., 2012). The Fe/Ca ratio is therefore used here as a semi-quantitative indicator of relative changes between terrigenous and carbonate contributions, which can help

reduce carbonate dilution effects in high-resolution environmental reconstructions (Zhang et al., 2023).

Fe/Ca ratios, however, can be influenced by non-climatic factors, including (i) physical and matrix effects associated with XRF-based measurements (e.g., variable water content, grain size, surface heterogeneity), (ii) shifts in sediment provenance and mineralogical composition, and (iii) redox-driven Fe remobilization and early diagenetic overprints (Weltje and Tjallingii, 2008; Hennekam and de Lange, 2012). Accordingly, Fe/Ca is treated as a semi-quantitative proxy and interpreted jointly with GR logs and lithologic observations. Integration with additional, process-specific proxies—such as stable isotopes ($\delta^{13}C$, $\delta^{18}O$), magnetic susceptibility, total organic carbon, grain size/mineralogy, and elemental ratios that track detrital input or redox (e.g., Ti/Al, Zr/Rb, Br, Mn/Fe)—has proven effective for paleoenvironmental reconstructions and for discriminating climatic forcing from non-climatic overprints (Last and Smol, 2001; Meyers et al., 2001; Croudace and Rothwell, 2015; Li et al., 2019).

Zircon U–Pb dating of tuffaceous layers within the Lower Wuerhe Formation on the northwestern margin of the Junggar Basin yields a youngest concordant age of 265.4 ± 3.5 Ma (Lu, 2018), which is used as the principal chronological tie point for anchoring the floating astronomical timescale constructed in this study.

3.2 Data preprocessing and spectral analysis

Time-series data (GR and Fe/Ca arranged by depth/time) were processed in Acycle 2.7. Prior to spectral analysis, we applied locally weighted scatterplot smoothing (LOWESS, 30% window) to remove the long-term trend while retaining orbital-scale variability. We then pre-whitened each series using an AR(1) model with parameters estimated from the data (median $\rho \approx 0.68$ across series) to reduce red noise and enhance cycle detection. Power spectra and evolutive spectra were computed using the multitaper method (MTM) and fast Fourier transform (FFT) (Ma et al., 2017; Kodama et al., 2014). Statistical significance against AR(1) red noise was assessed at 90%, 95%, and 99% confidence levels.

Sedimentation rates were estimated using correlation coefficient (COCO) and evolutionary COCO (eCOCO) methods with AR(1)-based red-noise modeling (Falahatkhah et al., 2022; Mann and Lees, 1996; Chen et al., 2022; Li et al., 2018a). Optimal rates were identified via F-tests, yielding 5.0–5.9 cm/ka. Based on these estimates, the theoretical 405 ka long-eccentricity target was converted into depth to locate the corresponding frequency range in the spectrum.

We used Gaussian band-pass filtering to extract the long-eccentricity component, setting the center frequency from the COCO/eCOCO-derived sedimentation rates and a relative bandwidth of ~20–25% of the center frequency to encompass the expected spread while minimizing overlap with adjacent bands. All preprocessing (detrending, pre-whitening, filtering) follows standard cyclostratigraphic practice (Li et al., 2018b; Gong and Li, 2019; Waltha, 2015). Because linear interpolation can smooth short-wavelength variability, interpretations of the highest frequencies are made cautiously; uneven-sampling methods (e.g., Lomb–Scargle) can be used as a robustness check on the original 2 m Fe/Ca series where needed.

3.3 Astronomical orbital parameters

The long eccentricity cycle at ~405 ka (corresponding to the g_2 – g_5 term), which arises primarily from secular gravitational interactions between Venus and Jupiter, is widely regarded as the most stable component of Earth's eccentricity spectrum over Phanerozoic timescales. Owing to its long-term stability and persistence in astronomical solutions, the ~405 ka cycle has been extensively used as a practical tuning target, often referred to as a “geological metronome,” in deep-time astrochronologic studies.

Although numerical integrations of the Solar System suggest that the amplitude of eccentricity terms may vary, and that orbital solutions become increasingly uncertain in deep time, the ~405 ka component remains the most robust and consistently identifiable eccentricity signal in sedimentary records. Consequently, it has been widely applied for astronomical tuning and time calibration in Paleozoic successions across diverse depositional settings, including both marine and lacustrine systems.

In late Paleozoic strata, Milankovitch-paced cyclicity has been documented in glacio-eustatic cyclothems as well as in non-glacial sedimentary archives, indicating that orbital forcing can be transferred into the stratigraphic record despite

potential non-stationarity in sedimentation rates and local depositional processes. For the Permian interval investigated here, theoretical orbital periods were adopted following deep-time astronomical estimates that explicitly consider uncertainties associated with chaotic behavior of the Solar System (e.g., Waltham, 2015) and previous Permian cyclostratigraphic applications in lacustrine basins (Bouilila et al., 2011).

Accordingly, the target orbital periods used in this study include long eccentricity (~405 ka), short eccentricity (~95 and ~125 ka), obliquity (~36.0–44.3 ka), and precession (~17.8–20.8 ka). These components yield an approximate hierarchical period ratio of 23.6: 7.03: 1.98: 1 (Table 2), which provides a reference framework for spectral identification, sedimentation-rate estimation, and astrochronologic interpretation.

3.4 Integrated prediction error filter analysis

Integrated Prediction Error Filter Analysis (INPEFA) is a log-based signal-processing technique derived from Prediction Error Filter Analysis (PEFA) and commonly applied in stratigraphic studies to enhance long- and short-term trends in well-log data. By cumulatively integrating prediction residuals, INPEFA highlights systematic changes in log behavior, such that inflection points or trend reversals in the INPEFA curve may correspond to stratigraphic turning points and candidate key surfaces.

INPEFA does not identify orbital periodicities directly; rather, it serves as an auxiliary tool for detecting stratigraphic trend changes and for supporting the delineation of cyclic boundaries inferred from independent spectral analyses. When used in conjunction with cyclostratigraphic results, INPEFA can improve recognition of high-frequency depositional rhythms and enhance well-to-well correlation, particularly in settings where lithologic contrasts are subtle or sedimentation rates vary.

In this study, INPEFA was applied to GR logs from the Lower Wuerhe Formation to assist in recognizing cycle boundaries and major stratigraphic trend changes identified through the spectral workflow (Section 3.2). Candidate high-frequency boundaries inferred from INPEFA were systematically compared with the band-pass-filtered ~405 ka eccentricity component and the resulting astrochronologic framework to ensure consistency between (i) log-based stratigraphic turning points and (ii) orbitally paced cyclicity.

In addition, INPEFA-assisted trend partitions were used to help locate flooding- and regression-related turning points within individual cycles (i.e., transitions between TST and RST) and to summarize longer-term stacking patterns at the third-order T–R sequence scale adopted in this study. In this way, INPEFA contributes to the integration of cyclostratigraphic signals with sequence-stratigraphic interpretation, while remaining constrained by the independently derived astronomical framework.

3.5 Astronomical signal validation

To test the consistency of extracted cycles with theoretical orbital periods, we applied correlation coefficient (COCO) and

TABLE 2 Theoretical Permian astronomical orbital periods and ratios.

| Ma | E/ka | e/ka | O/ka | P/ka | Data source |
|-----|------|---------|------------|------------|-----------------------|
| 270 | 405 | 125, 95 | 36.0, 44.3 | 17.8, 20.8 | Boulila et al. (2011) |
| 298 | 405 | 125, 95 | 35.5, 42.9 | 17.7, 20.6 | |
| 300 | 405 | 125, 95 | 35.5, 42.8 | 17.7, 20.6 | |

evolutionary COCO (eCOCO) analyses to the GR and Fe/Ca series using Permian orbital targets (Toucanne et al., 2009; Allen and Allen, 2013). Red-noise backgrounds were modeled with AR(1) processes whose parameters were estimated from each series (median $\rho \approx 0.68$), and significance was evaluated against the AR(1) null (Zhang et al., 2023; Weltje and Tjallingii, 2008). Given the depth-domain sampling interval of 0.125 m, the Nyquist wavenumber is 4 m^{-1} . Sedimentation rates from 0 to 7 cm/ka (0.1 cm/ka increments) were explored with 5,000 Monte Carlo simulations. We considered astronomical forcing to be supported where the null hypothesis (H0: no significant forcing) returned $H0\text{-SL} < 1\%$ within the expected target bands and where eCOCO indicated consistent, rate-stable plateaus across adjacent windows (Kodama et al., 2014). Target bands included long eccentricity (~ 405 ka), short eccentricity (100–130 ka), obliquity (36.0–44.3 ka), and precession (17.8–20.8 ka), allowing for the range expected in deep-time solutions (Table 2).

3.6 DYNOT sedimentary noise model

Sedimentary records contain not only orbitally paced signals but also variability generated by storms, floods, bioturbation, compaction, facies heterogeneity, and diagenetic overprints (Zhang et al., 2023; Chen et al., 2022; Gong and Li, 2019). The Dynamic Noise after Orbital Tuning (DYNOT) approach quantifies the relative contribution of such non-orbital variance through time by comparing the tuned signal to an AR(1) red-noise expectation and tracking deviations from orbital pacing (Gong and Li). DYNOT is descriptive rather than diagnostic of a single process; it summarizes the integrated effects of multiple sources of stratigraphic disturbance and incompleteness.

Here, DYNOT was calculated for the tuned GR and Fe/Ca time series to evaluate temporal changes in the stability of orbital-signal expression. We used a 1.2 Ma sliding window (approximately three long-eccentricity cycles), a 10 ka step size, and 5,000 Monte Carlo simulations to obtain robust estimates of noise-level variability. Higher DYNOT values indicate intervals with comparatively stronger non-orbital influence (e.g., increased event deposition, greater facies heterogeneity, or reduced accommodation/sedimentation continuity), whereas lower values suggest more regular, orbitally expressed deposition. Because multiple mechanisms can drive DYNOT variability, we interpret DYNOT primarily—as a relative index—in the context of independent observations (lithology, log trends, and the sequence-stratigraphic framework), rather than as a stand-alone environmental proxy.

4 Results

4.1 Astronomical cycle characteristics (spectral analysis and sedimentation rate)

To evaluate whether the Middle Permian Lower Wuerhe Formation preserves orbitally paced stratigraphic cyclicity, we analyzed untuned depth-domain gamma-ray (GR; 0.125 m sampling) and Fe/Ca (2 m sampling; resampled to 0.125 m only for plotting) series from well F7 using spectral approaches. Because Fe/Ca was originally sampled at 2 m (Nyquist wavenumber 0.25 m^{-1} ; Nyquist wavelength 4 m), it is insensitive to the shortest-wavelength variability; we therefore use Fe/Ca primarily as an independent check on the persistence and frequency structure of lower-frequency cyclicity identified in the GR record, rather than as a stand-alone high-frequency predictor. Apparent high-wavenumber features in Fe/Ca above 0.25 m^{-1} are interpreted as interpolation/aliasing artifacts and are not considered further.

Multitaper method (MTM) power spectra relative to an AR(1) red-noise background show multiple peaks above the 99% confidence level (Figures 3a,b). In the GR series, prominent peaks occur at ~ 0.040 , ~ 0.120 , ~ 0.520 , and $\sim 0.917 \text{ m}^{-1}$, corresponding to cycle thicknesses of ~ 25.0 , ~ 8.3 , ~ 1.92 , and ~ 1.09 m, respectively (Table 3). In the Fe/Ca series, significant low-wavenumber peaks occur at ~ 0.048 and $\sim 0.142 \text{ m}^{-1}$ (cycle thicknesses ~ 20.8 and ~ 7.0 m; Figure 3b and Table 4). Evolutive FFT spectra (Figures 3c,d) indicate that these bands are expressed through much of the interval, with modest drift in the mid-frequency band whose centroid lies between ~ 0.10 and $\sim 0.14 \text{ m}^{-1}$ across windows—consistent with non-stationary lacustrine–deltaic deposition.

Using the GR series, the dominant thickness ratios among the four bands are approximately 18.6–22.9: 6.3–7.6: 1.7–1.8: 1 when normalized to the shortest cycle. These ratios, together with the evolutive centroid of the mid-frequency band ($0.10\text{--}0.14 \text{ m}^{-1}$), broadly match theoretical period ratios for Permian long eccentricity (~ 405 ka), short eccentricity ($\sim 95\text{--}130$ ka), obliquity ($\sim 36\text{--}44$ ka), and precession ($\sim 18\text{--}21$ ka) (Tables 1, 2). The cross-proxy agreement in low-frequency peaks (GR and Fe/Ca), the persistence of spectral bands, and the approximate thickness-ratio concordance support an interpretation of Milankovitch-band forcing, while allowing for possible overprints by non-orbital processes.

Sedimentation rates were estimated by correlation coefficient (COCO) and evolutive COCO (eCOCO) analyses that compare observed depth-domain spectra with theoretical orbital targets (Figures 4a–j). Both datasets yield statistically

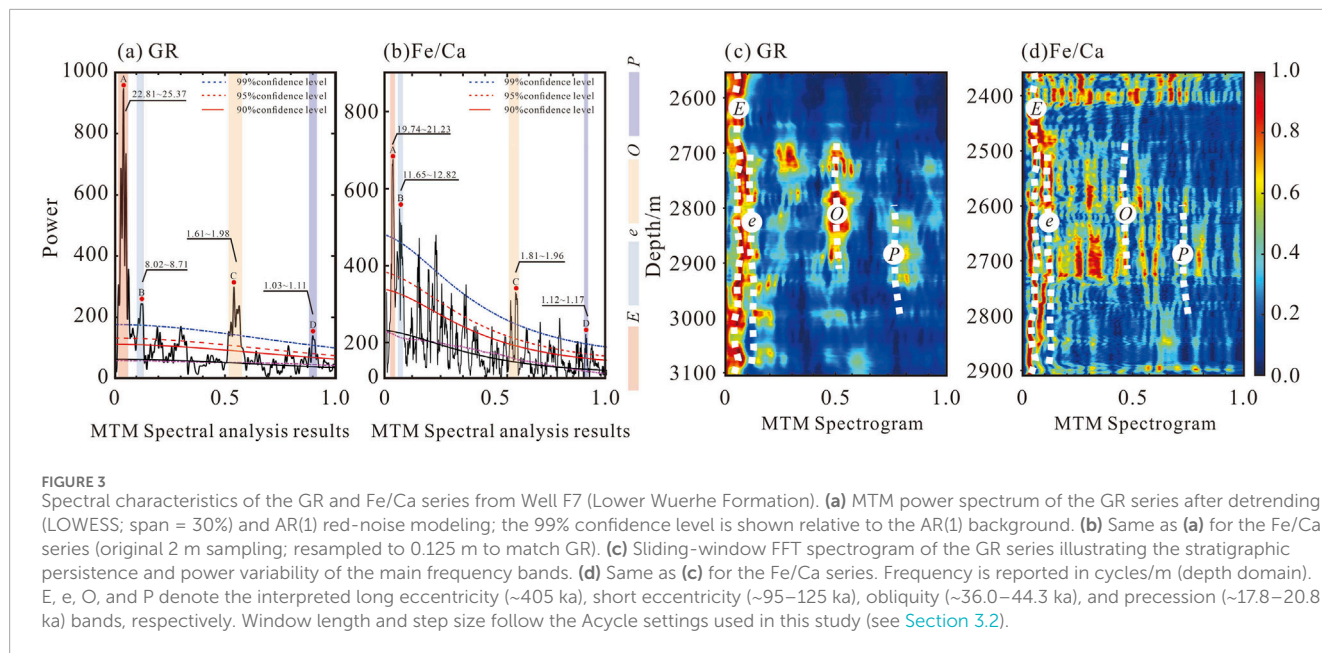


TABLE 3 Potential astronomical cycles identified in F7 well GR series, with cycle thicknesses and inferred sedimentation rates.

| Cycle type | Frequency(m ⁻¹) | Cycle thickness (m) | Thickness ratio (normalized) | Sedimentation rate (cm/ka) |
|-----------------------------------|-----------------------------|---------------------|------------------------------|----------------------------|
| E (Long eccentricity, 405 ka) | 0.04 | 25.00 | 22.87 | 6.17 |
| e (Short eccentricity, 95–125 ka) | 0.12 | 8.33 | 7.64 | 6.66–8.33 |
| O (Obliquity, 36.0–44.3 ka) | 0.52 | 1.92 | 1.76 | 4.47–5.49 |
| P (Precession, 17.8–20.8 ka) | 0.92 | 1.09 | 1 | 5.19–6.41 |

Cycle thickness is calculated as 1/frequency (cycles/m). Thickness ratios are normalized to the shortest cycle (P). Sedimentation rate ranges are calculated as cycle thickness divided by the corresponding theoretical orbital-period range (Table 2); therefore, the reported values represent plausible ranges rather than unique estimates.

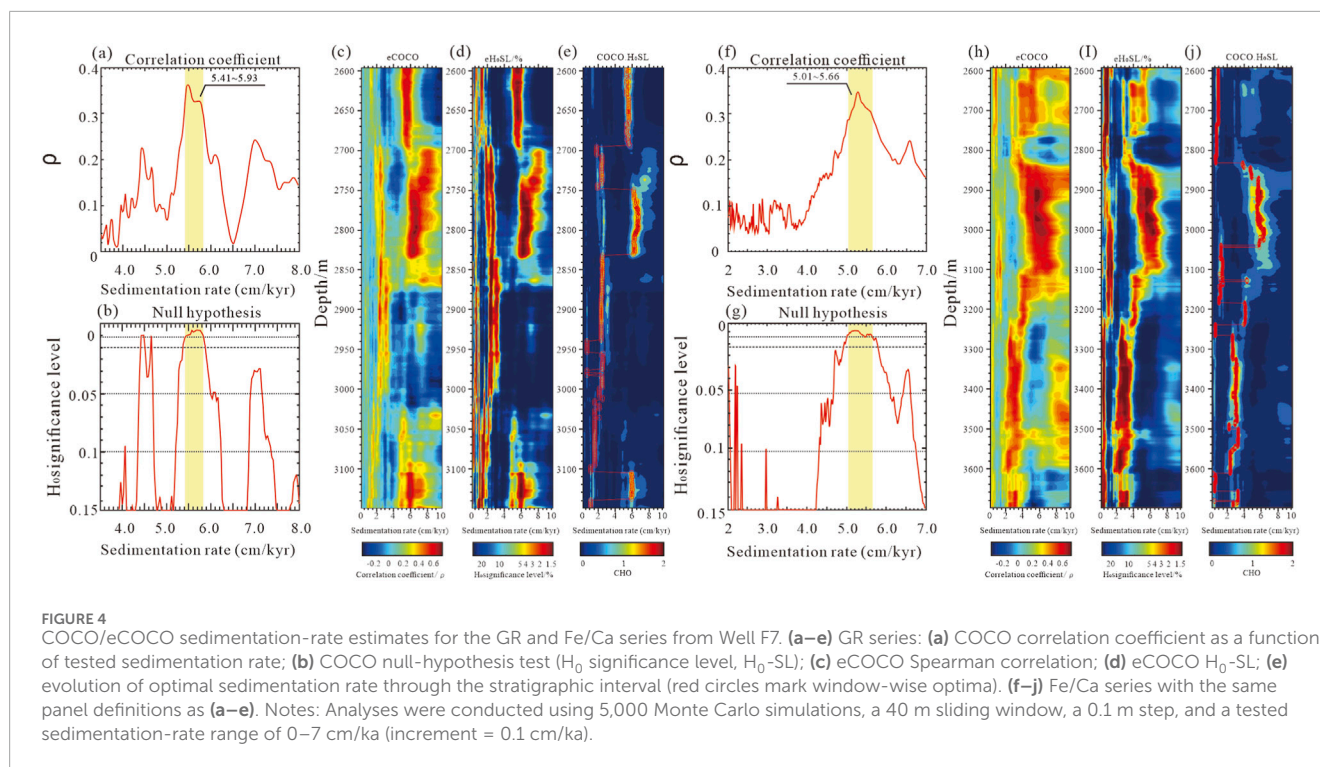
TABLE 4 Potential astronomical cycles identified in F7 well Fe/Ca series, with cycle thicknesses and inferred sedimentation rates.

| Cycle type | Frequency(m ⁻¹) | Cycle thickness (m) | Thickness ratio (normalized) | Sedimentation rate (cm/ka) |
|----------------------------------|-----------------------------|---------------------|------------------------------|----------------------------|
| E (Long eccentricity, 405 ka) | 0.05 | 20.83 | 18.59 | 5.10 |
| e(Short eccentricity, 95–125 ka) | 0.14 | 7.04 | 6.29 | 5.60–7.04 |
| O (Obliquity, 36.0–44.3 ka) | 0.53 | 1.89 | 1.69 | 4.39–5.40 |
| P (Precession, 17.8–20.8 ka) | 0.90 | 1.12 | 1 | 5.33–6.59 |

Cycle thickness is calculated as 1/frequency (cycles/m). Thickness ratios are normalized to the shortest cycle (P). Sedimentation rate ranges are calculated as cycle thickness divided by the corresponding theoretical orbital-period range (Table 2); therefore, the reported values represent plausible ranges rather than unique estimates.

significant correlations ($H_0-SL < 1\%$), with optimal sedimentation-rate windows of 5.41–5.93 cm/ka for GR and 5.01–5.66 cm/ka for Fe/Ca. The overlap between these independently derived windows supports the robustness of the orbital-frequency assignment. Using these rates, the GR peaks at ~25.0 m, ~1.92 m, and ~1.09 m convert to ~420–460 ka, ~32–36 ka, and ~18–22 ka, respectively—consistent with long eccentricity,

obliquity, and precession. The mid-frequency band's evolutive centroid (0.10–0.14 m⁻¹; ~7–10 m) converts to ~115–185 ka across the COCO/eCOCO windows; we interpret the lower portion of this range (~100–130 ka) as short eccentricity, with higher-thickness expressions reflecting temporal variability in sedimentation rate and spectral band broadening. Together, these results provide a quantitative basis for extracting the ~405 ka component and



constructing the astronomical age framework for the Lower Wuerhe Formation.

4.2 Astronomical timescale construction

Using the optimal sedimentation-rate window constrained by eCOCO (5.01–5.93 cm/ka; Section 4.1) and the clearer long-period expression in the GR record, Gaussian band-pass filters were applied to the GR and Fe/Ca depth series from well F7 to extract the ~ 405 ka long-eccentricity component. Because Fe/Ca was originally sampled at 2 m resolution, it is used here only to evaluate the consistency and phase stability of the long-eccentricity signal and not to define cycle boundaries independently. Filter center wavenumbers and bandwidths were selected within the COCO/eCOCO-constrained range for the 405 ka target (Figures 5b,f).

The filtered long-eccentricity component reveals eleven complete cycles (E1–E11) across the studied interval. To ensure reproducibility and minimize interpretational subjectivity, cycle boundaries were placed at a consistent phase of the filtered ~ 405 ka component (minima) and subsequently cross-checked against turning points in the INPEFA curve and stratigraphic/log features where available (Figures 5b,c,f–h). To mitigate edge effects, no boundaries were assigned within half a filter window from the series ends; only complete cycles well within the filtered interval were counted. As a robustness test, the filter center was varied within the COCO/eCOCO-constrained window and the relative bandwidth was adjusted (~ 20 – 25% of the center frequency); the resulting cycle count and boundary positions remained stable, with deviations limited to a small fraction of individual cycle thickness. Given the coarser sampling of Fe/Ca, its filtered ~ 405 ka component was used

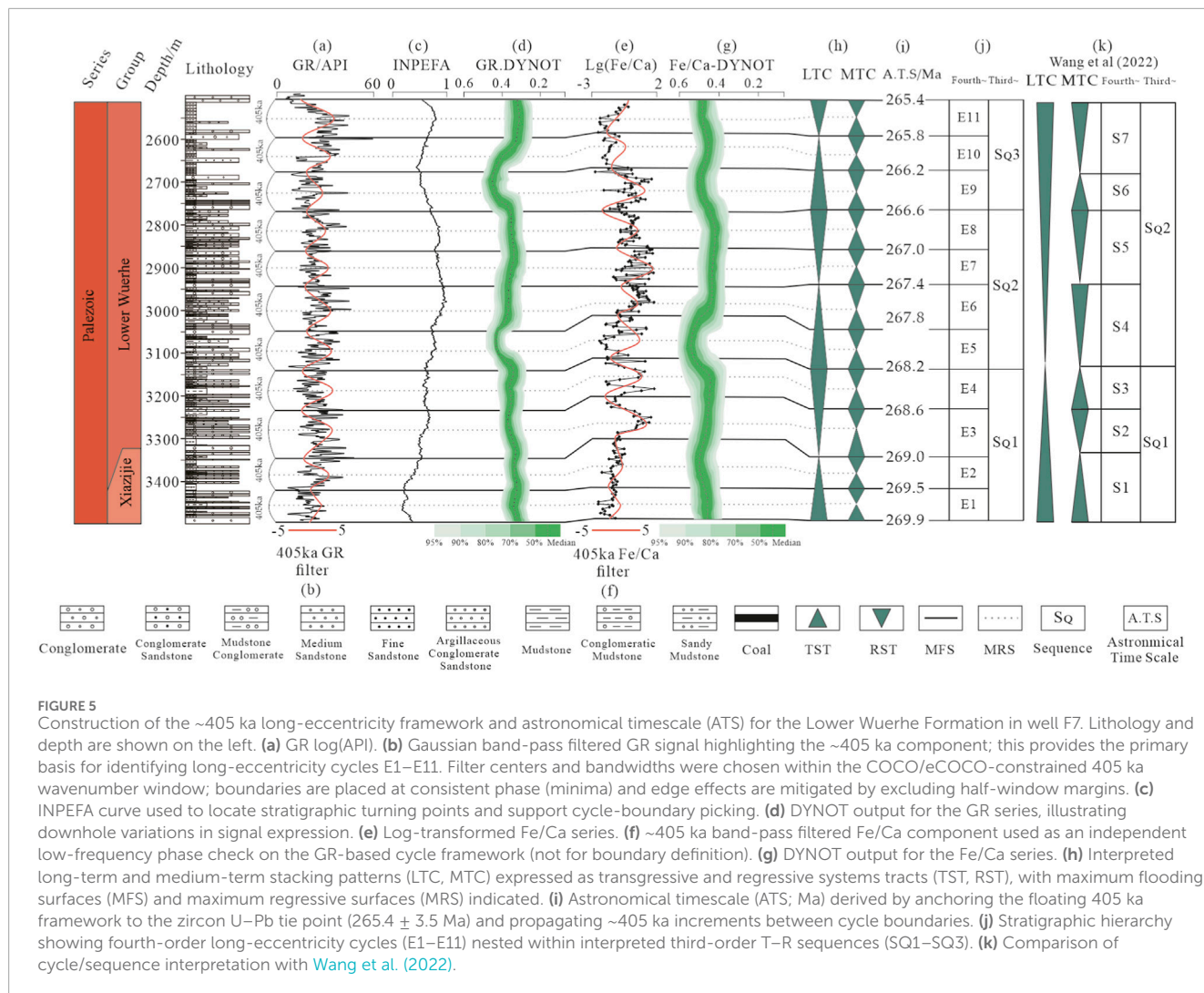
solely to verify phase consistency with the GR-derived signal rather than to refine boundary placement.

These eleven cycles define a floating astronomical timescale (ATS) for the Lower Wuerhe Formation. For absolute calibration, we adopted a published zircon U–Pb age of 265.4 ± 3.5 Ma from a tuffaceous horizon within the Lower Wuerhe Formation along the northwestern margin of the Junggar Basin (Lu, 2018). This dated horizon was correlated to well F7 using the integrated GR–Fe/Ca–INPEFA framework (Figure 5) and assigned an age of 265.4 Ma within the floating ATS. Ages for the remaining long-eccentricity cycle boundaries were then calculated by counting successive ~ 405 ka increments up- and down-section, yielding an astronomically calibrated age–depth model for well F7 (Figure 5i).

Absolute ages within the anchored ATS inherit uncertainty from the radiometric tie point (± 3.5 Ma), from potential minor departures from strictly uniform ~ 405 ka pacing, from filter-design choices, and from small boundary-picking uncertainties inherent to lacustrine–deltaic successions. Accordingly, the ATS is interpreted primarily as a high-resolution relative temporal framework, while absolute age placement is constrained by the available geochronologic control. Where spectral power weakens or lithologic evidence suggests condensation or minor omission, cycle boundaries were evaluated against independent stratigraphic criteria but were not forced to maintain idealized cycle regularity.

4.3 Super-long cycle (~ 1.2 Ma) identification

To probe longer-period modulation of the long-eccentricity signal, we computed the ratio of long-eccentricity band energy to total spectral energy (E/T) for the GR and Fe/Ca series from well

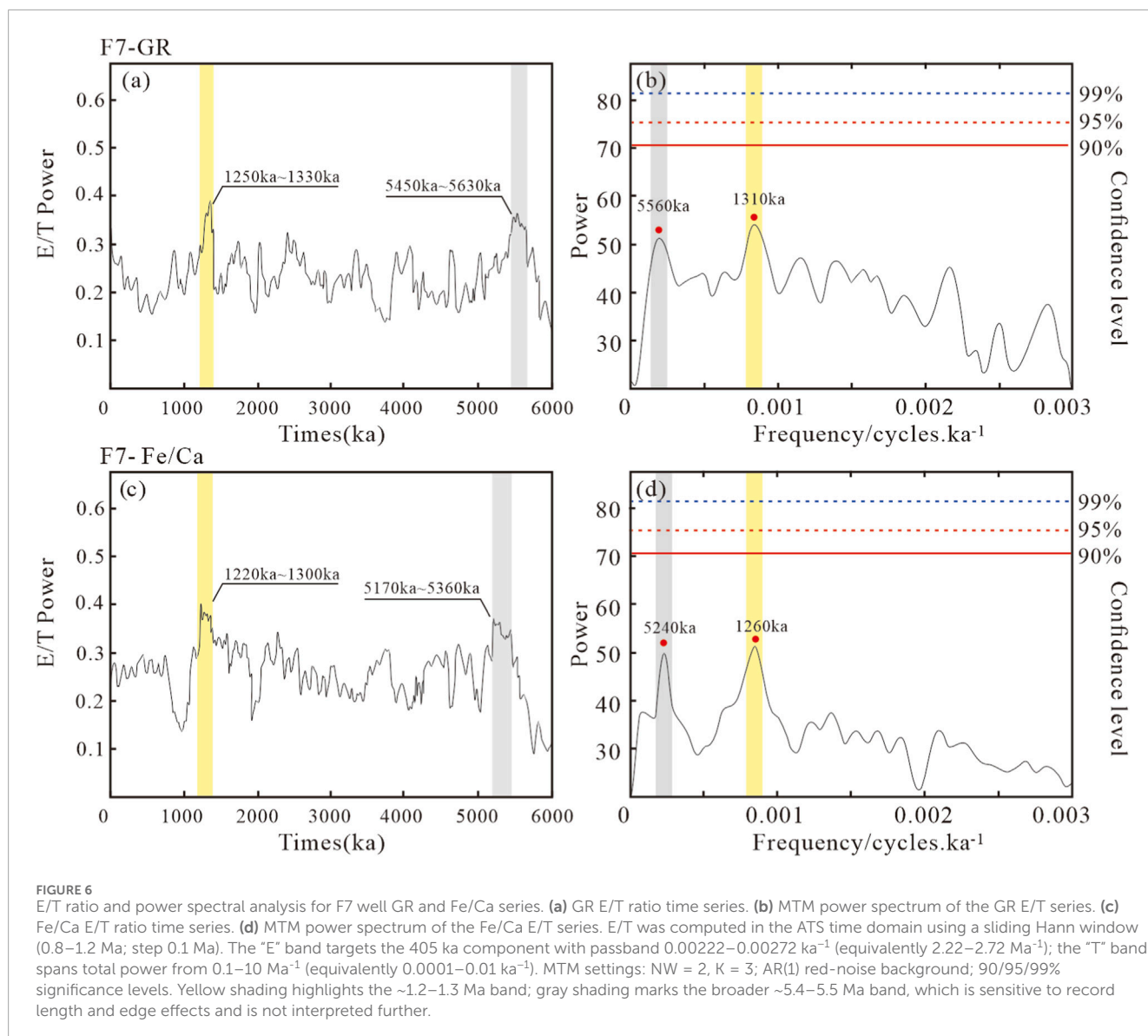


F7 (Figures 6a,c) and analyzed the resulting E/T series with power spectra (Figures 6b,d). In the GR-based E/T spectra, prominent peaks occur near ~1.31 Ma and ~5.50 Ma; the Fe/Ca-based E/T spectra yield peaks near ~1.26 Ma and ~5.40 Ma. The ~1.2–1.3 Ma signal is close to super-long obliquity modulation or higher-order eccentricity/obliquity interactions proposed for deep time and used in Permian applications (Toucanne et al., 2009; Allen and Allen, 2013). By contrast, the longer ~5.4–5.5 Ma feature exceeds the analyzed interval (~4.45 Ma; Section 4.2) and is sensitive to record length, edge effects, and bandwidth/leakage; we do not interpret it further.

The broadly similar ~1.2–1.3 Ma peaks in both proxies suggest that this signal is unlikely to be a single-dataset artefact. However, million-year-scale periodicities can arise from non-astronomical processes, including: (1) long-wavelength subsidence and accommodation variations driven by lithospheric flexure or dynamic topography (Cloetingh et al., 1999; Gurnis, 1993) (2) changes in sediment supply and source-to-sink signal propagation from surrounding orogenic belts (Armitage et al., 2011); and (3) autogenic organization in delta-lacustrine systems that generates stratigraphic cyclicity over 10^4 – 10^6 yr timescales

(Romans et al., 2016). Given the record length, the ~1.2–1.3 Ma peak spans ~3–4 modulation cycles and is resolvable, whereas the ~5.4–5.5 Ma feature is not (Jerolmack and Paola, 2010; Straub et al., 2020; Hajek and Straub, 2017).

Accordingly, we regard the ~1.2–1.3 Ma periodicity as a candidate modulation signal rather than a uniquely astronomical cycle, and we interpret it with caution. If at least partly astronomical, it could reflect obliquity-band amplitude modulation (the ~1.2 Ma obliquity envelope) interacting with eccentricity on Permian timescales, potentially amplified under late Paleozoic glacial boundary conditions (Mann and Lees, 1996; Li et al., 2018a). In this context, intermittent intensification of climate variability at ~1.2–1.3 Ma spacing could have influenced lake-level changes and sediment flux in the Mahu Sag, superimposed on the Milankovitch-scale (~405–17.8 ka) rhythms documented above. Distinguishing orbital from tectono-sedimentary controls on this super-long signal will require replication across multiple sections/wells, independent tectono-stratigraphic constraints, and modulation-specific tests (e.g., Hilbert amplitude envelopes of obliquity-band signals, evolutive coherency). We emphasize that no tuning or boundary placement was performed to this periodicity.



4.4 Sedimentary dynamics and noise response (DYNOT and INPEFA)

To evaluate how sedimentary dynamics and non-orbital processes modulated the expression of orbital-scale signals, we applied Integrated Prediction Error Filter Analysis (INPEFA; Figure 5c) and Dynamic Noise after Orbital Tuning (DYNOT; Figures 5d,g) to the GR and Fe/Ca series mapped into the astronomical timescale (ATS) constrained by the ~405 ka framework. DYNOT provides a relative measure of time-varying non-orbital variance; lower DYNOT values indicate intervals in which orbital pacing is more coherently expressed, whereas higher values reflect increased influence from event deposition, variable sedimentation rates, facies heterogeneity, or diagenetic overprints. Given the original 2 m sampling of Fe/Ca, DYNOT results from this proxy are interpreted only at lower frequencies and are used as an independent check on the GR-based patterns.

In the Lower Wuerhe Formation, pronounced DYNOT maxima occur at approximately 266.6 Ma and 268.2 Ma. These intervals coincide with elevated variance in both GR and Fe/Ca records and with stratigraphic characteristics consistent with relatively lower lake level and/or higher-energy depositional conditions, including enhanced clastic input and increased facies heterogeneity. In contrast, DYNOT minima correspond to intervals characterized by more uniform log responses and thicker fine-grained packages, consistent with more stable depositional conditions under which orbital pacing is more clearly expressed. Because DYNOT integrates the combined effects of multiple processes, these associations are interpreted as supportive rather than diagnostic and are evaluated in conjunction with lithologic observations and the sequence-stratigraphic context.

INPEFA highlights non-periodic, abrupt changes in GR log trends that mark stratigraphic turning points. Distinct negative inflections at approximately 265.4, 265.8, 266.2, 267.0, 267.4, 267.8, 268.6, 269.0, 269.5, and 269.9 Ma are interpreted as candidate

flooding-surface-type boundaries of high-frequency depositional cycles or as rapid environmental transitions. Final high-frequency depositional cycle (cycle set) boundaries were placed at a consistent phase of the filtered ~ 405 ka component (minima) and retained only where supported by coincident INPEFA turning points and stratigraphic/log evidence. Where spectral power weakens or facies evidence suggests condensation or minor omission, boundaries were not forced to maintain idealized regular spacing.

Taken together, DYNOT and INPEFA discriminate intervals dominated by relatively coherent orbital forcing from intervals characterized by stronger non-orbital noise and refine the placement of flooding-surface-bounded, high-frequency cycles within the cyclostratigraphic framework. We emphasize that DYNOT is used strictly as a relative index of noise intensity and that INPEFA serves as a trend-detection aid; neither method is used to infer orbital periods or to tune the record independently of the ~ 405 ka-anchored framework.

4.5 Astronomically calibrated stratigraphic framework and regional correlation

By integrating spectral results with the astronomically calibrated age-depth model, we established a hierarchical, astronomically constrained stratigraphic framework for well F7 (Figure 5j). Consistent with the T-R model defined in Section 1, three third-order transgressive-regressive sequences (SQ1-SQ3), bounded by maximum regressive surfaces (MRS), are delineated primarily from stacking patterns and key stratal surfaces in the logs. High DYNOT values and prominent INPEFA inflections, together with characteristic shifts in GR (and, at lower frequencies, Fe/Ca), provide supporting evidence that refines—but does not solely define—the placement of these sequence boundaries.

Within this framework, internal architecture is organized by orbital forcing. Each third-order sequence comprises a bundle of fourth-order, ~ 405 ka-paced high-frequency cycles that we treat as complete high-frequency depositional cycle (cycle set) bounded by flooding surfaces and their correlative surfaces. For visualization and regional reference (Figure 8), we use a nested notation: SQ1-1 to SQ1-4 (corresponding to E1-E4), SQ2-1 to SQ2-4 (E5-E8), and SQ3-1 to SQ3-3 (E9-E11). This hierarchy preserves the distinction between third-order T-R sequences and constituent fourth-order cycles; individual transgressive or regressive segments within a cycle are described as systems-tract components (TST/RST), not as separate “sequences.”

To test regional applicability, GR logs from wells F4, M1, and M2 were analyzed using MTM and FFT, revealing Milankovitch-band variance comparable to well F7 (Figure 7). Zero-phase Gaussian band-pass filtering of each well's GR data, using the ~ 405 ka passband constrained by that well's eCOCO sedimentation-rate window, highlights regionally coherent long-eccentricity cycles across the Mahu Sag (Figure 8). Guided by the continuity and phase stability of the ~ 405 ka band-pass filtered GR component, preliminary picks were placed at a consistent phase (minima). Final boundary placement, however, was anchored to GR-curve morphology and independently interpreted physical stacking patterns and key stratigraphic surfaces (MRS, MFS, and flooding surfaces), rather than to the filtered signal alone. Using this

procedure, the third-order T-R sequence boundaries and their internal fourth-order high-frequency depositional cycle (cycle set) boundaries from F7 were traced laterally to F4, M1, and M2. Where spectral power weakens or facies evidence suggests condensation/minor omission, boundaries were checked against independent criteria and not forced to maintain perfect regularity.

Correlations rely on continuity of cycle numbering (E1-E11; visualized as SQ1-1 to SQ3-3 in Figure 8), similarity in transgressive-regressive stacking trends, and alignment of near-isochronous flooding-surface-bounded cycles. Minor phase shifts or thickness variations between wells are attributed to spatial heterogeneity in sedimentation rates, accommodation, and sediment supply. The observed regional coherence confirms the robustness of the astronomically constrained framework for high-resolution, near-isochronous correlation and provides a quantitative temporal basis for paleogeographic analysis and exploration in the Mahu Sag.

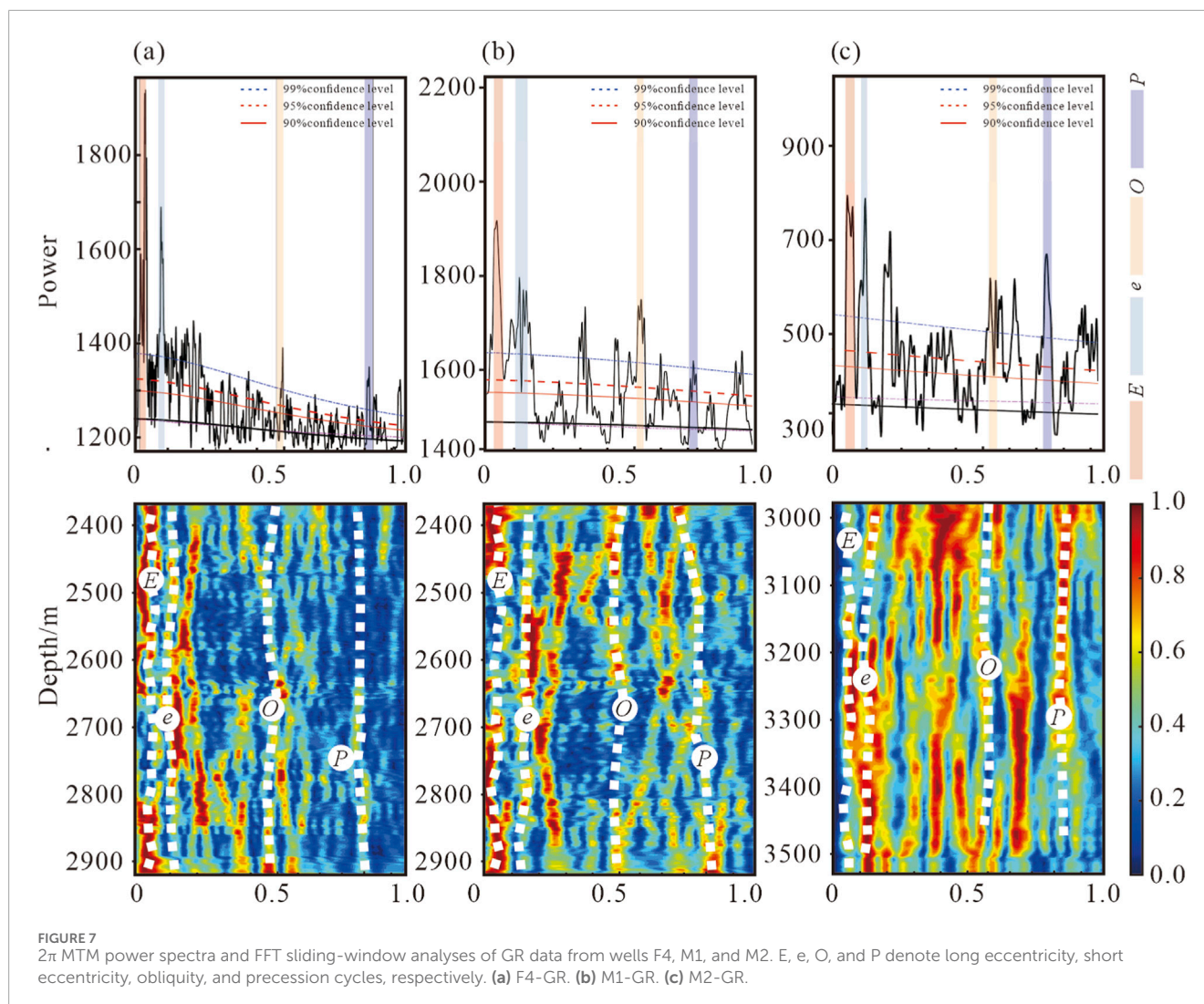
5 Discussion

5.1 Challenges in high-frequency sequence stratigraphy and contributions of cyclostratigraphy

In this study, we explicitly distinguish between cyclostratigraphic cycles and stratigraphic sequences to address the conceptual ambiguity often encountered in high-resolution stratigraphy. Specifically, orbital cycles, paced by Earth's orbital parameters, are treated as strict time-stratigraphic units used to construct an isochronous temporal framework. In contrast, sequence stratigraphy is applied to interpret the genetically related stacking patterns and accommodation changes within that temporal framework.

The precise delineation and correlation of high-frequency stratigraphic units remain significant challenges in sedimentology. A primary difficulty lies in defining objective, repeatable criteria for identifying boundaries that possess regional isochronous significance—a prerequisite for robust paleoenvironmental reconstruction and resource exploration. Traditional sequence-stratigraphic approaches excel at identifying major unconformities and maximum flooding surfaces (MFS) at lower frequencies (e.g., third-order). However, when applied to high-frequency (fourth-order or higher) intervals, purely lithological or surface-based correlations often suffer from interpretational subjectivity and the potential diachroneity of stratigraphic surfaces.

Cyclostratigraphy, by extracting periodic signals derived from Earth's orbital parameters (Milankovitch cycles), offers a “geological metronome” that significantly refines the resolution of stratigraphic analysis. Unlike lithological boundaries which may be influenced by local autogenic processes, astronomical tuning provides a mechanism to construct frameworks with both relative and absolute temporal precision. In this study, the integration of spectral analysis, COCO/eCOCO, Gaussian band-pass filtering, and INPEFA demonstrates how cyclostratigraphy can complement conventional sequence stratigraphy. By anchoring the third-order T-R sequences to a rigorous 405 ka long-eccentricity framework, we overcome the temporal uncertainties inherent



in traditional methods. This integrated approach results in a quantitatively calibrated, astronomically informed stratigraphic model for the Lower Wuerhe Formation, ensuring that high-frequency correlations are physically meaningful and temporally synchronous.

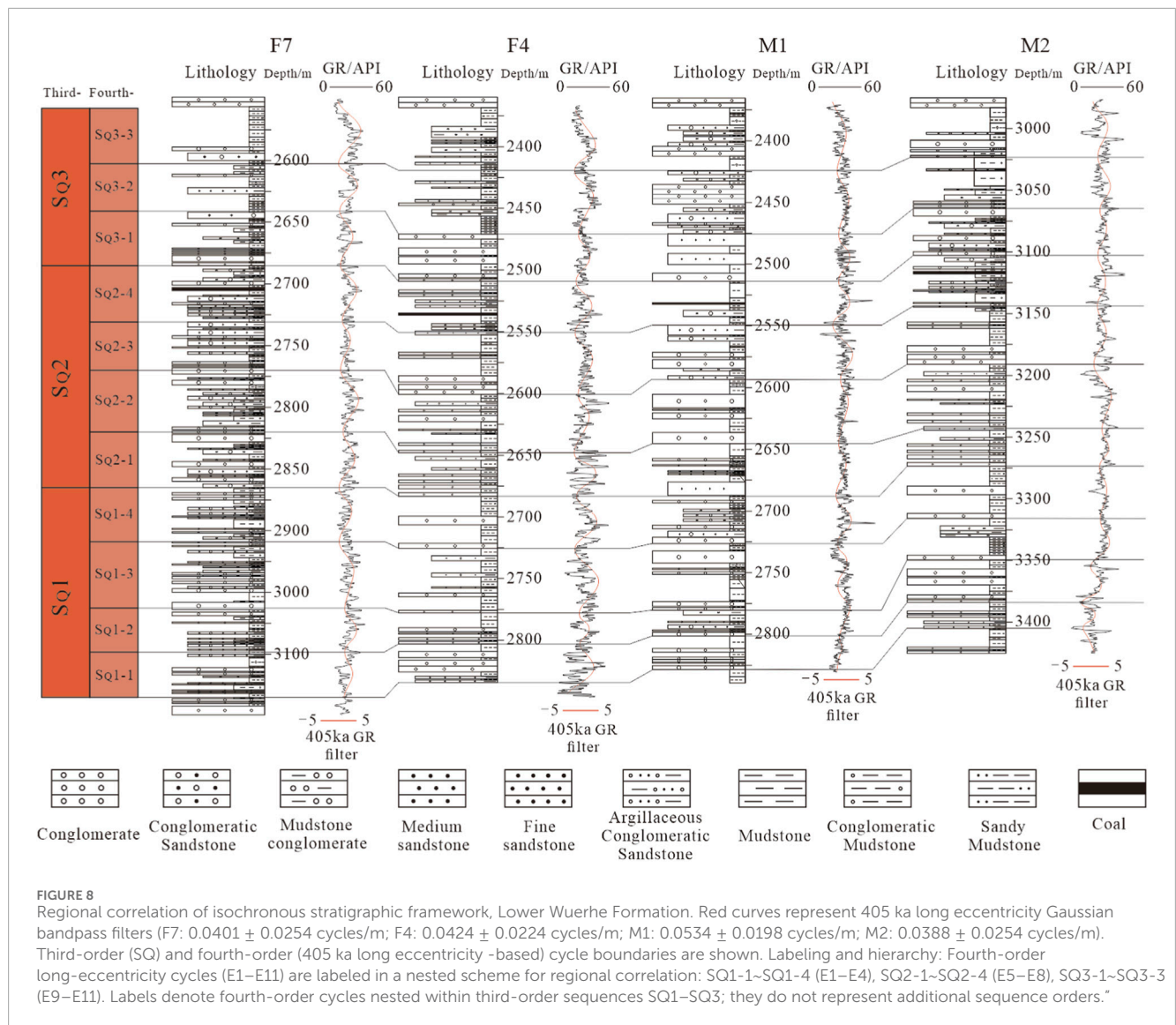
5.2 Comparison with previous studies and advances of this study

Previous sequence-stratigraphic studies of the Lower Wuerhe Formation in the Junggar Basin, such as Wang et al. (2022), identified two third-order sequences and seven fourth-order “sequences” [see Figure 5k in Wang et al. (2022)]. In contrast, the present study delineates three third-order sequences (SQ1–SQ3) and eleven fourth-order cycles paced by 405 ka long-eccentricity signals (Figure 5j). Notably, the SQ2 sequence of Wang et al. (2022) is subdivided here into two third-order sequences, with a boundary placed at 2675.4 m depth in well F7 (~265.4 Ma). This new boundary coincides with a peak in sedimentary noise in the DYNOT model and a marked inflection in the INPEFA curve. Furthermore,

based on lithologic transitions, GR and Fe/Ca curve morphology, and troughs in the 405 ka band-pass filtered data, the interval previously identified as the S1 “normal cycle” by Wang et al. (2022) is reinterpreted here as comprising two distinct components: a transgressive normal cycle (S1, fining-upward, bell-shaped GR curve) and a regressive inverse cycle (S2, coarsening-upward, funnel-shaped GR curve). Similarly, their S4, S5, and S7 inverse cycles are each subdivided into paired transgressive–regressive high-frequency cycles.

These differences reflect several methodological advances of the present study:

1. Multi-proxy and multi-well constraints. We integrate high-resolution GR logs from four wells (F7, F4, M1, M2) with Fe/Ca ratios from well F7 as a complementary, semi-quantitative environmental proxy. Although, as noted in Section 4.1, Fe/Ca ratios can be influenced by changes in provenance, redox conditions, and diagenetic overprinting, their cyclic variability—when interpreted in conjunction with GR and lithologic observations—provides an independent check on GR-derived cyclicity. The combined use of MTM,



FFT, eCOCO, Gaussian band-pass filtering, DYNOT, and INPEFA improves the detection of weak cycles, quantifies variations in sedimentation rates, and helps distinguish gradual environmental trends from abrupt depositional events, thereby enhancing the precision and robustness of cycle identification.

- High-resolution astronomical timescale anchored within the Lower Wuerhe Formation. By anchoring the 405 ka long-eccentricity cycles to a youngest concordant zircon U–Pb age of 265.4 Ma \pm 3.5 Ma obtained from a tuffaceous layer within the Lower Wuerhe Formation (Tang W. et al., 2021), this study constructs a high-resolution astronomical timescale (ATS) directly tied to the studied succession. This internal age anchor provides more reliable absolute temporal constraints and sedimentation-rate estimates than frameworks that lack precise age control or rely on ages from correlative but geographically distant formations. While we acknowledge that the ATS inherits uncertainties from the analytical error of the U–Pb age and possible minor departures from strictly

constant 405 ka pacing, it represents a significant refinement over previous models.

- Multi-proxy sequence-boundary identification. Third-order sequence boundaries (SQ1–SQ3) are defined using a robust combination of 405 ka long-eccentricity cycle signals, DYNOT-derived variations in signal preservation, INPEFA-indicated depositional discontinuities, and changes in GR, Fe/Ca, and lithofacies. This multi-proxy approach reduces the subjectivity associated with single-indicator methods and yields more objective and reproducible sequence-boundary interpretations.

5.3 Astronomical timescale and implications for regional correlation

This study estimates a depositional duration of \sim 4.45 Ma for the Lower Wuerhe Formation in well F7, based on eleven 405 ka long-eccentricity cycles identified through spectral analysis and Gaussian band-pass filtering. The astronomically calibrated

age–depth model provides a high-resolution temporal framework that allows quantitative assessment of tectonic subsidence rates, sediment flux, and the tempo of paleolake evolution. Spectral and filtering analyses of GR logs from wells F7, F4, M1, and M2 confirm that 405 ka long-eccentricity cycles are regionally consistent across the Mahu Sag (Figure 8), enabling the construction of an isochronous stratigraphic framework.

The quasi-constant, non-chaotic nature of the 405 ka long-eccentricity cycle in deep time (Ma et al., 2017) supports its reliability as a correlation tool in the Permian Junggar Basin and helps overcome the inherently non-isochronous character of traditional lithostratigraphic and seismic-reflection-based correlations. The resulting framework improves fine-scale reservoir correlation and paleogeographic reconstruction for hydrocarbon exploration.

At longer periods, the E/T spectra reveal ~1.2–1.3 Ma and ~5.4–5.5 Ma peaks (Figure 6), which may reflect super-long orbital modulation or grand cycles. However, the current chronological resolution, the limited number of dated horizons, and the potential for long-wavelength tectonic or sedimentary processes to generate similar periodicities prevent a unique attribution of these super-long signals to orbital forcing. Future studies should combine high-precision U–Pb dating (e.g., from multiple volcanic ash horizons), continuous magnetic susceptibility records, stable isotopes ($\delta^{18}\text{O}$, $\delta^{13}\text{C}$), and organic geochemical proxies to test the reproducibility, spatial extent, and origin of ~1.2–1.3 Ma and longer-period signals and to better distinguish between orbital and tectonic controls.

5.4 Geological significance of the ~1.2–1.3 Ma super-long cycle

The identification of a 1.2–1.3 Ma peak in the E/T ratio spectra (Figure 6) offers a potential window into the lower-frequency pacing of the Mahu Sag's evolution. As discussed in Section 4.3, while non-astronomical factors such as basin subsidence or autogenic feedbacks cannot be ruled out, the signal's periodicity aligns with theoretical expectations for super-long obliquity modulation (Falahatkhah et al., 2022; Mann and Lees, 1996). In the context of the Early Permian (Asselian–Sakmarian) late Paleozoic ice age (Tang W. et al., 2021), such a modulation could have driven periodic intensifications of climate variability, regulating sediment supply and water balance in the lacustrine system on a million-year scale.

Stratigraphically, this 1.2–1.3 Ma modulation appears to provide a low-frequency context that influences the stacking patterns of the third-order sequences. Phases of higher E/T values (stronger eccentricity/obliquity variance) generally correspond to intervals of deeper lacustrine conditions, characterized by enhanced accommodation space and potentially better organic matter preservation. Conversely, phases of lower E/T values tend to coincide with periods of deltaic progradation and increased clastic input. This relationship suggests that the super-long cycle, regardless of its ultimate origin (orbital vs. tectonic), played a role in organizing the large-scale distribution of reservoir sands versus source rocks within the Lower Wuerhe Formation.

However, we maintain a cautious interpretation. Given the tectonic proximity to the evolving Hercynian orogenic belt,

the observed signal likely records a complex interplay between orbital climate forcing and regional tectonic pulses. Therefore, while the 1.2–1.3 Ma periodicity provides a useful descriptive framework for characterizing long-term stratigraphic trends, we do not yet utilize it as a primary tool for high-resolution correlation. Future work integrating extensive spatial sampling with independent tectonic modeling is required to disentangle the relative contributions of astronomical versus tectonic controls in this interval.

5.5 Limitations and future directions

Despite the advances in cycle identification and sequence delineation, several limitations remain:

1. Age control. The ATS is anchored to a single in-situ zircon U–Pb age of 265.4 ± 3.5 Ma obtained from a tuffaceous horizon within the Lower Wuerhe Formation. Although this represents a significant improvement over frameworks anchored to external formations, the reliance on one dated level means that absolute ages of individual sequence boundaries still carry uncertainties related to analytical error, the stratigraphic distance from the dated horizon, and assumptions about constant 405 ka pacing. Additional high-precision U–Pb ages from multiple stratigraphic levels within or immediately adjacent to the Wuerhe Formation would substantially improve the absolute temporal calibration.
2. Sedimentation-rate variability. eCOCO provides robust estimates of average sedimentation rates for different intervals, but spatial and temporal variability in sedimentation remains. Localized changes in accommodation, sediment supply, or depositional processes can cause deviations from the average rates implied by the astronomical tuning. Future studies could employ higher-resolution analyses (e.g., focusing on precession-scale cycles) and forward stratigraphic or stochastic modeling to better quantify dynamic sedimentation-rate changes and their impact on cycle preservation.
3. Fe/Ca proxy complexity. Fe/Ca ratios reflect the combined effects of climate-driven changes in weathering and runoff and non-climatic factors such as provenance shifts, redox conditions, basin chemistry, and diagenetic alteration. Although Fe/Ca provides useful complementary information when interpreted together with GR and lithology, additional proxies—such as stable isotopes ($\delta^{13}\text{C}$, $\delta^{18}\text{O}$), magnetic susceptibility, and organic geochemical indicators (e.g., TOC, biomarkers)—are needed to more robustly separate climatic from non-climatic influences.
4. Spatial coverage. This study focuses on four wells in the Mahu Sag, which may not capture the full range of facies and tectonic conditions in the Junggar Basin. Extending cyclostratigraphic and astrochronologic analyses to other sub-basins and margins of the Junggar Basin would test the regional applicability of the proposed astronomical framework and help identify lateral variations in sequence architecture and sedimentary response to orbital forcing.

Future research should integrate seismic-stratigraphic, paleontological, paleomagnetic, and geochemical data to build a

more comprehensive, multi-scale stratigraphic framework. High-precision U–Pb dating from multiple horizons, combined with magnetic susceptibility, stable isotope, and organic geochemical records, will be critical for validating the presence and origin of super-long (~1.2–1.3 Ma and longer) cycles and for disentangling the relative roles of climatic versus tectonic controls. Such integrated approaches will further enhance the utility of the astronomically calibrated stratigraphic framework for both hydrocarbon exploration and paleoenvironmental reconstruction in the Junggar Basin.

6 Conclusion

Through detailed cyclostratigraphic analysis of GR and Fe/Ca data from well F7, supplemented by regional well comparisons (F4, M1, M2) in the Mahu Sag, Junggar Basin, this study yields the following conclusions.

1. Milankovitch-driven sedimentation. MTM spectral analysis of the GR and Fe/Ca series identifies statistically significant power peaks corresponding to ~405 ka long eccentricity, ~95–125 ka short eccentricity, ~36.0–44.3 ka obliquity, and ~17.8–20.8 ka precession cycles. COCO/eCOCO analyses confirm stable coupling between these orbital periods and the observed stratigraphic rhythms, indicating that astronomical forcing played a primary role in controlling sedimentation of the Lower Wuerhe Formation.
2. High-resolution astronomical timescale anchored within the Lower Wuerhe Formation. Eleven 405 ka long-eccentricity cycles, anchored to a youngest concordant zircon U–Pb age of 265.4 ± 3.5 Ma from a tuffaceous horizon within the Lower Wuerhe Formation, define an astronomically calibrated timescale (ATS) spanning ~4.45 Ma for the studied interval in well F7. This internally anchored ATS provides improved constraints on absolute ages and sedimentation rates, while still inheriting uncertainties from the analytical error of the U–Pb age and possible minor deviations from perfectly constant 405 ka pacing.
3. Super-long modulation and hierarchical sequence framework. A ~1.2–1.3 Ma peak in the E/T ratio spectra of both GR and Fe/Ca series is interpreted as a candidate super-long modulation of the long-eccentricity signal that may influence third-order sequence stacking patterns. Combined with DYNOT-derived noise trends and INPEFA-detected discontinuities, three third-order sequences (SQ1–SQ3) and eleven fourth-order cycles (E1–E11) are delineated. Because million-year-scale periodicities can also arise from tectonic or sedimentary processes, the ~1.2–1.3 Ma signal is interpreted with caution and is not used as a standalone correlation tool.
4. Regional correlation and implications. The 405 ka long-eccentricity-based stratigraphic framework exhibits consistent sequence boundaries, cycle geometries, and stacking patterns across wells F7, F4, M1, and M2. This regional coherence validates the astronomically calibrated framework as a reliable isochronous correlation tool for fine-scale stratigraphy, paleoenvironmental analysis, and reservoir prediction in the Mahu Sag, and provides a robust temporal basis for future

paleogeographic reconstruction and hydrocarbon exploration in the Junggar Basin.

Data availability statement

Publicly available datasets were analyzed in this study. This data can be found here: [10.6084/m9.figshare.30815507](https://doi.org/10.6084/m9.figshare.30815507).

Author contributions

WY: Conceptualization, Data curation, Formal Analysis, Investigation, Methodology, Visualization, Writing – original draft, Writing – review and editing. GY: Conceptualization, Data curation, Project administration, Resources, Writing – original draft. JL: Formal Analysis, Resources, Supervision, Writing – review and editing. SY: Conceptualization, Data curation, Writing – review and editing. JY: Funding acquisition, Resources, Software, Writing – review and editing.

Funding

The author(s) declared that financial support was received for this work and/or its publication. From the Tianshan Talent Project of Xinjiang Uygur Autonomous Region under the grant number 2023TSYCJC0010.

Acknowledgements

We would like to express our sincere gratitude to the staff of the Fengcheng Institute of Geology, Xinjiang Oilfield Company for their strong support and assistance during the sample collection process. We are also deeply thankful to the experts who engaged in academic exchanges with the authors via email and provided valuable insights on technical details. Their help has been instrumental in the smooth progress and successful completion of this research.

Conflict of interest

Authors WY, GY, JL, and SY were employed by Xinjiang Oilfield Company.

The remaining author(s) declared that this work was conducted in the absence of any commercial or financial relationships that could be construed as a potential conflict of interest.

Generative AI statement

The author(s) declared that generative AI was not used in the creation of this manuscript.

Any alternative text (alt text) provided alongside figures in this article has been generated by Frontiers with the support of artificial intelligence and reasonable efforts have been made to ensure accuracy, including review by the authors wherever possible. If you identify any issues, please contact us.

Publisher's note

All claims expressed in this article are solely those of the authors and do not necessarily represent those of their affiliated

organizations, or those of the publisher, the editors and the reviewers. Any product that may be evaluated in this article, or claim that may be made by its manufacturer, is not guaranteed or endorsed by the publisher.

References

- Allen, P. A., and Allen, J. R. (2013). *Basin analysis: principles and application to petroleum play assessment*. 3rd ed. Wiley-Blackwell. doi:10.1002/9781118450314
- Armitage, J. J., Duller, R. A., Whittaker, A. C., and Allen, P. A. (2011). Buffering of fluvial sediment transport waves by the stratigraphic record. *Nat. Geosci.* 4 (7), 446–450. doi:10.1038/ngeo1193
- Baddouh, M., Meyers, S. R., Carroll, A. R., Beard, B. L., and Johnson, C. M. (2016). Lacustrine $^{87}\text{Sr}/^{86}\text{Sr}$ as a tracer to reconstruct milankovitch forcing of the Eocene hydrologic cycle. *Earth Planet Sci. Lett.* 448, 141–153. doi:10.1016/j.epsl.2016.05.007
- Boulika, S., Galbrun, B., Miller, K. G., Stephen, F. P., James, V. B., Laskar, J., et al. (2011). On the origin of Cenozoic and Mesozoic 'third-order' eustatic sequences. *Earth Sci. Rev.* 109 (3–4), 94–112. doi:10.1016/j.earscirev.2011.09.003
- Boulika, S., Galbrun, B., Huret, E., Hinnov, L. A., Rouget, I., Gardin, S., et al. (2014). Astronomical calibration of the Toarcian stage: implications for sequence stratigraphy and duration of the early Toarcian OAE. *Earth Planet Sci. Lett.* 386, 98–111. doi:10.1016/j.epsl.2013.10.047
- Cao, H., Jin, S., Hou, M., Chen, S., Liu, Y., and Chen, A. (2022). Astronomical cycles calibrated the sea-level sequence durations of late Miocene to Pliocene in Qiongdongnan Basin, South China Sea. *Mar. Pet. Geol.* 143, 105813. doi:10.1016/j.marpetgeo.2022.105813
- Catuneanu, O. (2019). Scale in sequence stratigraphy. *Mar. Pet. Geol.* 106, 125–138. doi:10.1016/j.marpetgeo.2019.04.026
- Catuneanu, O., Abreu, V., Bhattacharya, J. P., Blum, M. D., Dalrymple, R. W., Eriksson, P. G., et al. (2009). Towards the standardization of sequence stratigraphy. *Earth Sci. Rev.* 92 (1–2), 1–33. doi:10.1016/j.earscirev.2008.10.003
- Catuneanu, O., Martins-Neto, M. A., and Eriksson, P. G. (2012). Sequence stratigraphic framework and application to the Precambrian. *Mar. Pet. Geol.* 33 (1), 8–25. doi:10.1016/j.marpetgeo.2010.10.002
- Chen, Z., Li, F., and Zhang, P. (2022). High-resolution terrestrial record of orbital climate forcing in the coal-bearing Middle Jurassic Yan'an formation, ordos basin, North China. *Geol. J.* 57 (5), 1873–1890. doi:10.1002/gj.4385
- Cheng, H., Li, H., Sha, L., Sinha, A., Shi, Z., Yin, Q., et al. (2022). Milankovitch theory and monsoon. *Innovation.* 3 (6), 100338. doi:10.1016/j.xinn.2022.100338
- Cloetingh, S., Burov, E., and Poliakov, A. (1999). Lithosphere folding: primary response to compression? *Tectonics.* 18 (6), 1064–1083. doi:10.1029/1999TC900040
- Crampton, J. S., Meyers, S. R., Cooper, R. A., Sadler, P. M., Foote, M., and Harte, D. (2018). Pacing of paleozoic macroevolutionary rates by Milankovitch grand cycles. *Proc. Natl. Acad. Sci. U. S. A.* 115 (22), 5686–5691. doi:10.1073/pnas.1714342115
- Croudace, I. W., and Rothwell, R. G. (2015). *Micro-XRF studies of sediment cores: applications of a non-destructive tool for the environmental sciences* (Dordrecht: Springer). doi:10.1007/978-94-017-9849-5
- Dang, W., Gao, G., You, X., Wu, J., Liu, S., Yan, Q., et al. (2023). Genesis and distribution of oils in Mahu Sag, Junggar Basin, NW China. *Pet. Explor. Dev.* 50 (4), 721–735. doi:10.1016/S1876-3804(23)60432-X
- Embry, A. F. (1993). Transgressive-regressive (T-R) sequence analysis of the Jurassic succession of the Sverdrup basin, Canadian arctic archipelago. *Can. J. Earth Sci.* 30 (2), 301–320. doi:10.1139/e93-024
- Embry, A. F. (2002). "Transgressive-regressive (T-R) sequence stratigraphy," in *Sequence stratigraphic models for exploration and production: evolving methodology, emerging models and application case histories* (GCSSEPM Foundation 22nd Annual Research Conference), Houston, TX: GCSSEPM Foundation, 151–172. doi:10.5724/gcs.02.22.0151
- Falahatkah, O., Kordi, M., Fatemi, V., and Koochi, H. H. (2022). Recognition of milankovitch cycles during the oligocene-early Miocene in the zagros basin, SW Iran: implications for paleoclimate and sequence stratigraphy. *Sediment. Geol.* 440, 106261. doi:10.1016/j.sedgeo.2021.105957
- Gong, Z. (2021). Cyclostratigraphy of the Cryogenian fiq formation, Oman, and its implications for the age of the marinoan glaciation. *Glob. Planet Change.* 204, 103584. doi:10.1016/j.gloplacha.2021.103584
- Gong, Z., and Li, M. S. (2019). Astrochronology of the Ediacaran shuram carbon isotope excursion, Oman. *Earth Planet Sci. Lett.* 547, 116462. doi:10.1016/j.epsl.2019.116462
- Govin, A., Holzwarth, U., Heslop, D., Keeling, L. D., Zabel, M., Mülitz, S., et al. (2012). Distribution of major elements in Atlantic surface sediments (36°N–49°S): imprint of terrigenous input and continental weathering. *Geochem Geophys Geosyst.* 13 (1), Q01013. doi:10.1029/2011GC003785
- Gurnis, M. (1993). Phanerozoic marine inundation of continents driven by dynamic topography above subducting slabs. *Nature.* 364 (6438), 589–593. doi:10.1038/364589a0
- Hajek, E. A., and Straub, K. M. (2017). Autogenic sedimentation in clastic stratigraphy. *Annu. Rev. Earth Planet Sci.* 45, 681–709. doi:10.1146/annurev-earth-063016-015935
- Hennekam, R., and de Lange, G. J. (2012). X-ray fluorescence core scanning of wet marine sediments: methods to improve quality and reproducibility of high-resolution paleoenvironmental records. *Limnol. Oceanogr. Methods.* 10, 991–1004. doi:10.4319/lom.2012.10.991
- Hou, M. G., Zha, M., Ding, X. J., Yin, H., Bian, B. L., Liu, L. H., et al. (2021). Source and accumulation process of Jurassic biodegraded oil in the eastern Junggar Basin, NW China. *Pet. Sci.* 18 (3), 721–735. doi:10.1016/j.petsci.2021.07.010
- Jerolmack, D. J., and Paola, C. (2010). Shredding of environmental signals by sediment transport. *Geophys. Res. Lett.* 37 (19), L19401. doi:10.1029/2010GL044638
- Kemp, D. B., and Van Manen, S. M. (2019). Metre-scale cycles in shallow water carbonate successions: milankovitch and stochastic origins. *Sedimentology.* 66 (7), 2638–2660. doi:10.1111/sed.12609
- Kodama, K. P., and Hinnov, L. A. (2014). *Rock magnetic cyclostratigraphy*. Hoboken NJ: Wiley. doi:10.1002/9781118561294
- Kodama, K. P., and Hinnov, L. A. (2014). "Doing rock magnetic cyclostratigraphy," in *New analytical methods in earth and environmental science series*. Editor L. A. Hinnov (Hoboken, NJ: Wiley-Blackwell). doi:10.1002/9781118561294.ch7
- Lachniet, M., Asmerom, Y., Polyak, V., and Denniston, R. (2017). Arctic cryosphere and milankovitch forcing of great basin paleoclimate. *Sci. Rep.* 7, 13653. doi:10.1038/s41598-017-13279-2
- Laskar, J., Robutel, P., Joutel, F., Gastineau, M., Correia, A. C. M., and Levrard, B. (2004). A long-term numerical solution for the insolation quantities of the Earth. *Astron. Astrophys.* 428 (1), 261–285. doi:10.1051/0004-6361:20041335
- Laskar, J., Fienga, A., Gastineau, M., and Manche, H. (2011). La2010: a new orbital solution for the long-term motion of the Earth. *Astron. Astrophys.* 532, A89. doi:10.1051/0004-6361/201116836
- Last, W. M., and Smol, J. P. (2001). "Tracking environmental change using Lake sediments," *Physical and geochemical methods* (Kluwer Academic Publishers), 2. doi:10.1007/0-306-47670-3
- Lei, D., Abulimiti, B., Tang, Y., Chen, J., and Cao, J. (2014). Controlling factors and occurrence prediction of high oil-gas production zones in Lower Triassic baikouquan formation of Mahu Sag in Junggar Basin. *Xinjiang Pet. Geol.* 35 (5), 495. Available online at: <https://www.zgxpjg.com/EN/Y2014/V35/I5/1>.
- Li, M., Huang, C., Hinnov, L. A., Ogg, J., Chen, Z., and Zhang, Y. (2016). Obliquity-forced climate during the early Triassic hothouse in China. *Geology.* 44 (8), 623–626. doi:10.1130/G37970.1
- Li, M., Kump, L. R., Hinnov, L. A., and Mann, M. E. (2018a). Tracking variable sedimentation rates and astronomical forcing in Phanerozoic paleoclimate proxy series with evolutionary correlation coefficients and hypothesis testing. *Earth Planet Sci. Lett.* 501, 165–179. doi:10.1016/j.epsl.2018.08.041
- Li, M., Hinnov, L. A., Huang, C., and Ogg, J. G. (2018b). Sedimentary noise and sea levels linked to land-ocean water exchange. *Nat. Commun.* 9, 1004. doi:10.1038/s41467-018-03454-y
- Li, M., Hinnov, L. A., and Kump, L. (2019). Acycle: time-series analysis software for paleoclimate research and education. *Comput. Geosci.* 127, 1–11. doi:10.1016/j.cageo.2019.02.011
- Li, W., Zhang, J., Xie, J., Xia, Y., and He, Y. (2023). Application of the wavelet transform and INPEFA in sequence stratigraphy. *ACS Omega.* 8 (3), 3441–3451. doi:10.1021/acsomega.2c07367
- Li, X., Chen, G., Wu, C., Li, J., Haproff, P. J., Geng, M., et al. (2023). Tectono-stratigraphic framework and evolution of East Junggar Basin, Central Asia. *Tectonophysics.* 851, 229758. doi:10.1016/j.tecto.2023.229758
- Liu, X., Ge, J., Qu, H., and Ma, C. (2024). Sequence stratigraphy driven by tectonic subsidence and astronomical forcing: a case study from the Miocene Pearl River Mouth Basin, South China Sea. *Mar. Pet. Geol.* 107, 107074. doi:10.1016/j.marpetgeo.2024.107074

- Lu, Y. (2018). *Permian chrono-stratigraphic framework and sedimentary filling evolution of the Mahu-Shawan area*. (Beijing: China University of Geosciences). Available online at: https://kns.cnki.net/kcms2/article/abstract?v=dzw7IdLhHkG0coshqFgFkEBqq_gM7y17tu0nQ4xMOaLTfnCehW1cHtFh_d1JMdE9xd2LXPFq_Tu8Y oBxxZGkdxQLyGu1Uu3wBlfMEaONrz6gfXBqoUtkEVrwQaflbbsqnUA19djhJfWXdp648LGswfvNC6goiVBBfYJ8JQgJjQjQwd44MnMnAyJB7IXl87xFj&uniplatform=NZKPT&language=CHS.
- Ma, C., and Li, M. (2020). Astronomical time scale of the Turonian constrained by multiple paleoclimate proxies. *Geosci. Front.* 11 (4), 1489–1500. doi:10.1016/j.gsf.2020.01.013
- Ma, C., Meyers, S. R., and Sageman, B. B. (2017). Theory of chaotic orbital variations confirmed by Cretaceous geological evidence. *Nature* 542 (7642), 468–470. doi:10.1038/nature21402
- Ma, K., Hinnov, L. A., Zhang, X., and Gong, Y. (2020). Astronomical time calibration of the Upper Devonian lali section, South China. *Glob. Planet Change* 193, 103267. doi:10.1016/j.gloplacha.2020.103267
- Mann, M. E., and Lees, J. M. (1996). Robust estimation of background noise and signal detection in climatic time series. *Clim. Change* 33, 409–445. doi:10.1007/BF00142586
- Meyers, P. A., and Teranes, J. L. (2001). "Sediment organic matter," in *Tracking environmental change using Lake sediments. Volume 2: physical and geochemical methods*. Editors W. M. Last, and J. P. Smol (Kluwer Academic Publishers), 239–269. doi:10.1007/0-306-47670-3_9
- Miall, A. D., and Miall, C. E. (2001). Sequence stratigraphy as a scientific enterprise: the evolution and persistence of conflicting paradigms. *Earth Sci. Rev.* 54 (4), 321–348. doi:10.1016/s0012-8252(00)00041-6
- Peterson, L. C., Haug, G. H., Hughen, K. A., and Rohl, U. (2000). Rapid changes in the hydrologic cycle of the tropical Atlantic during the last glacial. *Science*. 290 (5498), 1947–1951. doi:10.1126/science.290.5498.1947
- Romans, B. W., Castellort, S., Covault, J. A., Fildani, A., and Walsh, J. P. (2016). Environmental signal propagation in sedimentary systems across multiple scales of analysis. *Earth-Sci. Rev.* 153, 7–29. doi:10.1016/j.earscirev.2015.07.012
- Ruhl, M., Hesselbo, S. P., Hinnov, L., Jenkyns, H. C., Xu, W., Riding, J. B., et al. (2016). Astronomical constraints on the duration of the early Jurassic Pliensbachian stage and global climatic fluctuations. *Earth Planet Sci. Lett.* 455, 149–165. doi:10.1016/j.epsl.2016.08.038
- Schlager, W. (2004). Fractal nature of stratigraphic sequences. *Geology*. 32 (3), 185–188. doi:10.1130/G20253.1
- Schnyder, J., Ruffell, A., Deconinck, J. F., and Baudin, F. (2006). Conjunctive use of spectral gamma-ray logs and clay mineralogy in defining late Jurassic–early Cretaceous palaeoclimate change (Dorset, U.K.). *Palaeogeogr. Palaeoclimatol. Palaeoecol.* 229 (1–2), 303–320. doi:10.1016/j.palaeo.2005.06.027
- Slatt, R. M., and Rodriguez, N. D. (2012). Comparative sequence stratigraphy and organic geochemistry of gas shales: commonality or coincidence? *J. Nat. Gas. Sci. Eng.* 8, 68–84. doi:10.1016/j.jngse.2012.01.008
- Strasser, A., Hilgen, F. J., and Heckel, P. H. (2006). Cyclostratigraphy: concepts, definitions, and applications. *Newslett. Stratigr.* 42 (2), 75–114. doi:10.1127/0078-0421/2006/0042-0075
- Straub, K. M., Duller, R. A., Foreman, B. Z., and Hajek, E. A. (2020). Buffering of external signals by autogenic processes in fluvio-deltaic stratigraphy: a review of experimental results. *Sedimentology*. 67 (2), 783–825. doi:10.1111/sed.12600
- Tang, Y., Cao, J., He, W., Shan, X., Liu, Y., Zhao, K., et al. (2021). Development tendency of geological theory of total petroleum system: insights from the discovery of Mahu large oil province. *Xinjiang Pet. Geol.* 42 (1), 1–9. Available online at: <https://www.zgxjg.com/EN/Y2021/V42/I1/1>.
- Tang, W., Zhang, Y., Pe-Piper, G., Piper, D. J. W., Guo, Z., and Li, W. (2021). Permian to early Triassic tectono-sedimentary evolution of the Mahu Sag, Junggar Basin, Western China: sedimentological implications of the transition from rifting to tectonic inversion. *Sediment. Geol.* 399, 1–18. doi:10.1016/j.marpetgeo.2020.104730
- Tian, J., Wu, H., Huang, C., Li, M., Ma, C., and Wang, P. (2022). Revisiting the Milankovitch theory from the perspective of the 405-ka long eccentricity cycle. *Earth Sci. J. China Univ. Geosci.* 47 (10), 3543–3561. doi:10.3799/dqkx.2022.248
- Toucanne, S., Zaragosi, S., Bourillet, J. F., Gibbard, P. L., Eynaud, F., Giraudeau, J., et al. (2009). A 1.2 Ma record of glaciation and fluvial discharge from the West European Atlantic margin. *Quat. Sci. Rev.* 28 (25–26), 2974–2981. doi:10.1016/j.quascirev.2009.08.003
- VanderPlas, J. T. (2018). Understanding the lomb-scargle periodogram. *Astrophys. J. Suppl. Ser.* 236 (1), 1–16. doi:10.3847/1538-4365/aab766
- Waltham, D. (2015). Milankovitch period uncertainties and their impact on cyclostratigraphy. *J. Sediment. Res.* 85 (8), 990–998. doi:10.2110/jsr.2015.66
- Wang, Y., Xiong, W., Yu, H., Zhang, K., and Zhang, G. (2022). Sequence stratigraphic framework and sedimentary filling model of lucaogou formation in eastern Junggar Basin. *Pet. Geol. Recover. Eff.* 29 (04), 12–24. doi:10.13673/j.cnki.cn371359/TE.202106048
- Wang, R., Chen, X., Chang, Q., and Zhao, X. (2024). Identification of milankovitch sedimentary cycle in Fengcheng Formation, Mahu depression: a case study of well maye 1. *Front. Earth Sci.* 12, 1390929. doi:10.3389/feart.2024.1390929
- Weltje, G. J., and Tjallingii, R. (2008). Calibration of XRF core scanners for quantitative geochemical logging of sediment cores: theory and application. *Earth Planet Sci. Lett.* 274 (3–4), 423–438. doi:10.1016/j.epsl.2008.07.054
- Wong, R. E. (2021). A modified Milankovitch theory that reconciles contradictions with the paleoclimate record. *Clim. Past.* 17 (2), 421–439. doi:10.5194/cp-2021-10
- Wu, H., Zhang, S., Hinnov, L. A., Jiang, G., Feng, Q., Li, H., et al. (2013). Time-calibrated Milankovitch cycles for the late Permian. *Nat. Commun.* 4, 2452. doi:10.1038/ncomms3452
- Xu, J., Liu, L., Qin, Y., and Zhang, J. (2015). Frequency trend attribute analysis for stratigraphic division and correlation. *Geophysics*. 80 (1), A1–A13. doi:10.1190/geo2013-0304.1
- Xu, X. W., Jiang, N., Li, X. H., Wu, C., Qu, X., Zhou, G., et al. (2015). Spatial-temporal framework for the closure of the Junggar Ocean in central Asia: new SIMS zircon U–Pb ages of the ophiolitic mélange and collisional igneous rocks in the Zhifang area, East Junggar. *J. Asian Earth Sci.* 111, 471–487. doi:10.1016/j.jseas.2015.06.017
- Yang, W., Feng, Q., Liu, Y., Tabor, N., Miggins, D., Crowley, J. L., et al. (2010). Depositional environments and cyclo- and chronostratigraphy of uppermost carboniferous–lower Triassic fluvial–lacustrine deposits, southern Bogda Mountains, NW China—A terrestrial paleoclimatic record of mid-latitude NE Pangea. *Glob. Planet Change*. 73 (1–2), 15–113. doi:10.1016/j.gloplacha.2010.03.008
- Zhang, R., Kemp, D. B., Thibault, N., Jelby, M. E., Li, M., Huang, C., et al. (2023). Astrochronology and sedimentary noise modeling of Pliensbachian (Early Jurassic) sea-level changes, Paris Basin, France. *Earth Planet Sci. Lett.* 614, 118199. doi:10.1016/j.epsl.2023.118199
- Zhao, K., Du, X., Lu, Y., Xiong, S., and Wang, Y. (2019). Are light-dark coupled laminae in lacustrine shale seasonally controlled? a case study using astronomical tuning from 42.2 to 45.4 Ma in the Dongying depression, Bohai Bay Basin, eastern China. *Palaeogeogr. Palaeoclimatol. Palaeoecol.* 528, 45–57. doi:10.1016/j.palaeo.2019.04.034
- Zhao, J., Chen, S., Deng, G., Shao, X., Zhang, H., Aminov, J., et al. (2019). Basement structure and properties of the Western Junggar Basin, China. *J. Earth Sci.* 30 (2), 255–268. doi:10.1007/s12583-018-1207-4